A confined–unconfined aquifer model for subglacial hydrology and its application to the North East Greenland Ice Stream

Sebastian Beyer[1,2], Thomas Kleiner[2], Vadym Aizinger[2,3], Martin Rückamp[2], and Angelika Humbert[2,4]

[1]Potsdam Institute for Climate Impact Research, Potsdam, Germany
[2]Alfred Wegener Institute, Helmholtz Centre for Polar and Marine Research, Bremerhaven, Germany
[3]Friedrich–Alexander University Erlangen–Nürnberg, Erlangen, Germany
[4]University of Bremen, Bremen, Germany

Correspondence to: Sebastian Beyer (sebastian.beyer@awi.de)

Abstract. Subglacial hydrology plays an important role in the ice sheet dynamics as it determines the sliding velocity of ice sheets. It also drives freshwater into the ocean, leading to undercutting of calving fronts by plumes. Modeling subglacial water has been a challenge for decades, and only recently new approaches have been developed such as representing subglacial channels and thin water sheets by separate layers of variable hydraulic conductivity. We extend this concept by modeling a confined and unconfined aquifer system (CUAS) in a single layer. The advantage of this formulation is that it prevents unphysical values of pressure at reasonable computational cost. We also performed sensitivity tests to investigate the effect of different model parameters. The strongest influence of model parameters was detected in terms governing the opening and closure of channels. Furthermore, we applied the model to the North East Greenland Ice Stream, where an efficient system independent of seasonal input was identified about $500\,\mathrm{km}$ downstream from the ice divide. Using the effective pressure from the hydrology model in the Ice Sheet System Model (ISSM) showed considerable improvements of modeled velocities in the coastal region.

1 Introduction

Subglacial water has been identified as a key component in glacial processes, it is fundamental in driving large ice flow variations over short time periods. Recent studies show considerable progress in modeling these subglacial networks and coupling them to ice models. Water pressure strongly influences basal sliding and can therefore be considered a fundamental control on ice velocity and ice-sheet dynamics (Lliboutry, 1968; Röthlisberger, 1972; Gimbert et al., 2016).

Generally, two fundamentally different types of drainage are identified: discrete channel / conduit systems and distributed water sheets or thin films. Distributed flow mechanisms are, for example, linked cavities (Lliboutry, 1968), flows through sediment/till (Hubbard et al., 1995), or thin water sheets (Weertman, 1957); those are considered to be an inefficient and slow system to transport water. Channels (Rothlisberger, 1969; Shreve, 1972; Nye, 1976) are seen as discrete single features or

arborescent networks; they usually develop over the summer season when a lot of melt water is available. It is assumed that these channelized or efficient drainage systems able to drain large amounts of water in short time spans are predominant in alpine glaciers and on the margins of Greenland, where substantial amounts of surface melt water are capable of reaching the bed (van den Broeke et al., 2017). In the interior of Greenland and also in most parts of Antarctica, the water supply is limited to melt due to the geothermal and frictional heating within the ice (Aschwanden et al., 2016) – a circumstance favoring distributed systems.

Seasonal variations of ice velocity have been observed and attributed to the evolution of the drainage system switching between an efficient and inefficient state in summer and winter (Bartholomew et al., 2010). For this reason, a new generation of subglacial drainage models has been developed recently that is capable of coupling the two regimes of drainage and reproducing the transition between them (Schoof, 2010; Hewitt et al., 2012; Hewitt, 2013; Werder et al., 2013; De Fleurian et al., 2014; Hoffman and Price, 2014). While these models demonstrate immense progress for modeling spontaneously evolving channel networks, it is still a challenge to apply them on a continental scale. A comprehensive overview of the various operational and newly emerging glaciological hydrology models is given in Flowers (2015).

Distributed or sheet structures can naturally be well represented using a continuum approach, while channels usually require a secondary framework, where each feature is described explicitly. Water transport in channels is a complex mechanism that depends on the balance of melt and ice creep (Nye, 1976; Rothlisberger, 1969), channel geometry, and network topology. Additionally, the network evolves over time which further complicates modeling of this process. When simulating channel networks particular care must be also taken to prevent the emergence of instabilities due to runaway merging of channels (see the discussion in Schoof et al. (2012)). This leads to increased modeling complexity and high computational costs. An exception to this is the work of De Fleurian et al. (2014), where both systems are represented by Darcy flow through separate porous media layers. The layer representing the channels has its parameters (namely hydraulic conductivity and storage) adjusted to exhibit the behavior of an effective system.

We take this idea even further and only use a single layer of Darcy flow with locally adjusted transmissivity of the layer at locations where channels form, while, at the same time, accounting for a decrease in storage. This means that we approximate the channel flow as a fast diffusion process similarly to work in De Fleurian et al. (2014); however, a single Darcy flow layer with spatially varying parameters (effective hydraulic conductivity) accounts for both drainage mechanisms. Similar approaches are known to have been applied to modeling of fracture networks in rock Van Siclen (2002). This reduced complexity model does not capture channels individually but represents their effect by changing specific local properties. Since our model aims to simultaneously represent the main properties of both drainage mechanisms (efficient and inefficient), special care must be exercised when choosing the model parameters and relating them to the physical properties of a specific scenario. While this strategy may not help to advance the precise understanding of channel formation processes, it captures the overall behavior and allows to examine the complex interactions on larger spatial and temporal scales. Currently we focus on channelised hydrology, whereas in future we will consider to expand the model towards cavity formation and closure. This is primarily due to the fact that cavity formation is not considered a dominant effect underneath the large ice sheets (Fowler, 1987).

In addition, we introduce a new Confined–Unconfined Aquifer Scheme (CUAS) that differentiates between confined and unconfined flow in the aquifer (Ehlig and Halepaska, 1976). While the assumption of always saturated – and therefore confined – aquifers may be true for glaciers with large water supply, it does not hold in areas with lower water input. Especially in locations far from the coast, the water supplies are often insufficient to completely fill the aquifer. Ignoring this leads to significant errors in the computed hydraulic potential and unphysical, i.a. negative, water pressure. This problem has been analyzed in detail by Schoof et al. (2012), but here we study the effect in the context of equivalent aquifer models using unconfined flow as a possible solution.

Large scale ice flow models often compute the basal velocity using a Weertman-type sliding law, where the inverse of the effective pressure (difference between ice overburden pressure and water pressure) determines the velocity at the base. Low effective pressure leads to high basal velocity. Without subglacial hydrology models, the ice models simply take the ice overburden pressure as effective pressure completely neglecting water pressure. This is a major reason why these models struggle to represent fast flowing areas such as ice streams. The effective pressure computed by our model can be easily coupled to an ice sheet model and improve results for fast flowing areas.

The following work is structured as follows. In the next section, we present the one-layer model of subglacial aquifer and briefly describe its discretization. In Sect. 3 the model is applied to artificial scenarios, and the sensitivity to model parameters and stability are investigated. In addition, results for seasonal forcing are presented there, and we show how the model evolves over time. Section 4 demonstrates the first application of the proposed methodology to the North East Greenland Ice Stream (NEGIS), which is the only interior ice stream in Greenland. It penetrates far into the Greenland mainland with its onset close to the ice divide, so sliding apparently plays a major role in its dynamics. A short conclusions and outlook section wraps up the present study.

2 Methods

2.1 Confined–Unconfined Aquifer Scheme

The vertically integrated continuity equation in combination with Darcy's law leads to the general *groundwater flow equation* (see e.g. Kolditz et al. (2015)):

$$S\frac{\partial h}{\partial t} = \nabla \cdot (T\nabla h) + Q \tag{1}$$

with S the storage coefficient (change in the volume of stored water per unit change of the hydraulic head over a unit area), h the hydraulic head (water pressure in terms of water surface elevation above an arbitrary datum; piezometric head), T transmissivity of the porous medium, and Q the source term. For a confined aquifer, $T = Kb$, where K is the hydraulic conductivity, and b is the aquifer thickness. $S = S_s b$ with specific storage S_s given by

$$S_s = \rho_{\mathrm{w}}\omega g\left(\beta_{\mathrm{w}} + \frac{\alpha}{\omega}\right) \tag{2}$$

with material parameters for the porous medium (porosity ω, compressibility α) and water (density ρ_{w}, compressibility β_{w}).

3

In order to consider the general form covering both cases (confined and unconfined), we follow Ehlig and Halepaska (1976) and write the general form for the confined–unconfined problem:

$$S_e(h)\frac{\partial h}{\partial t} = \nabla \cdot (T(h)\nabla h) + Q. \tag{3}$$

Now the transmissivity and the storage coefficient depend on the head and are defined as

$$T(h) = \begin{cases} Kb, & h \geq b & \text{confined} \\ K\Psi, & 0 \leq h < b & \text{unconfined} \end{cases} \tag{4}$$

where $\Psi = h - z_b$ is the the local height of the head over bedrock z_b and effective storage coefficient S_e is given by

$$S_e(h) = S_s b + S'(h) \tag{5}$$

with

$$S'(h) = \begin{cases} 0, & b \leq \Psi & \text{confined,} \\ (S_y/d)(b - \Psi), & b - d \leq \Psi < b & \text{transition,} \\ S_y, & 0 \leq \Psi < b - d & \text{unconfined.} \end{cases} \tag{6}$$

This means that as soon as the head sinks below the aquifer height, the system becomes unconfined, and therefore only the saturated section contributes to the transmissivity calculation. This also prevents the head from falling below the bedrock as detailed in Section 3.2. Additionally, the mechanism for water storage changes from elastic relaxation of the aquifer (confined) to dewatering under the forces of gravity (unconfined). The amount of water released from dewatering is described by the specific yield S_y. Since this amount is usually orders of magnitudes larger than the release from confined aquifer ($S_y \gg S_s b$), it is useful to introduce a gradual transition as in Eq. (6) controlled by a user defined transition parameter d.

Note that the transmissivity is not homogeneous making Eq. (3) nonlinear. This fits with our approach to describe the effective system (channels) by locally increasing the hydraulic conductivity. The benefit of this approach is discussed in Sect. 3.2.

Water pressure P_w and effective pressure N are related to hydraulic head as

$$P_\mathrm{w} = \Psi \rho_\mathrm{w} g \tag{7}$$

and

$$N = P_\mathrm{i} - P_\mathrm{w} \tag{8}$$

with g acceleration due to gravity, $P_\mathrm{i} = \rho_\mathrm{i} g H$ the cryostatic ice overburden pressure exerted by ice with thickness H and density ρ_i.

2.2 Opening and closure

Opening and closure of channels is governed by melt at the walls due to the dissipation of heat and the pressure difference between the inside and outside of the channel leading to creep deformation. We follow de Fleurian et al. (2016) in using the
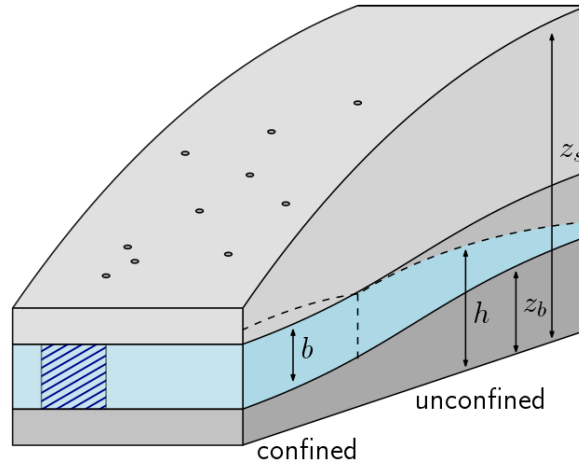
Figure 1. Schematics of the confined–unconfined aquifer scheme and artificial geometry for experiments. The hatched zone represents an area where the system is efficient. Dots on top indicate moulins.

classical channel equations from Nye (1976) and Röthlisberger (1972) to scale our transmissivity in order to reproduce this behavior. In contrast to de Fleurian et al. (2016), we do not evolve the aquifer thickness but the conductivity K, which leads to

$$\frac{\partial K}{\partial t} = v_{\text{melt}} - v_{\text{creep}},\tag{9}$$

in which

$$v_{\text{melt}} = \frac{rg\rho_{\text{w}}\min\left(b,\Psi\right)K}{\rho_{\text{i}}L}(\nabla h)^2 \tag{10}$$

and

$$v_{\text{creep}} = 2An^{-n}|N|^{n-1}NK \tag{11}$$

with L the latent heat, r roughness factor, A the creep rate factor depending on temperature, and n the creep exponent, which we choose as $n = 3$. Depending on the sign of N, creep closure as well as creep opening can occur. Negative effective pressure over prolonged time is usually considered unphysical, and the correct solution to this would be to allow the ice to separate from the bed (see e.g. Schoof et al. (2012) for a possible solution). However, in the context of our equivalent layer model, Eq. (11) is still applicable because this is how a channel would behave for $N < 0$. In Sect. 3.1, we test the sensitivity of K and N to the magnitudes of r and A.

3 Experiments with artificial geometries

Testing out equivalent layer model and finding parameters for it is not straightforward because there are no directly comparable physical properties. Moreover, observations and measurements of subglacial processes are in general difficult and sparse.

We address this by testing the model with some of the benchmark experiments of the **S**ubglacial **H**ydrology **M**odel **I**nter-comparison **P**roject (shmip.bitbucket.io).

The proposed artificial geometry mimics a land-terminating ice sheet margin measured $100\,\text{km}$ in the x-direction and $20\,\text{km}$ in the y-direction. The bedrock is flat ($z_b(x,y) = 0\,\text{m}$) with the terminus located at $x = 0$ while the surface z_s is defined by a square root function $z_s(x,y) = 6\left((x+5e3)^{1/2} - (5e3)^{1/2}\right) + 1$. Here, we use the SHMIP/B2 setup, which includes 10 moulins with constant in time supply. Boundary conditions are set to zero influx at the interior boundaries ($y = 0$, $y = 20$, $x = 100$) and zero effective pressure at the terminus. All experiments start with initial conditions that imply zero effective pressure and are run for 50 years to ensure that they reach a steady state.

3.1 Parameter estimation and sensitivity

SHMIP is primarily intended as a qualitative comparison between different subglacial hydrology models, where results from the GlaDS model (Werder et al., 2013) serve as a "common ground". Here, we use it as a basis for an initial tuning and a study of the sensitivity of our model with regard to parameters. The upcoming results from the SHMIP are also the reason why we do not show a comparison to other models in this study but refer to the manuscript in preparation instead.
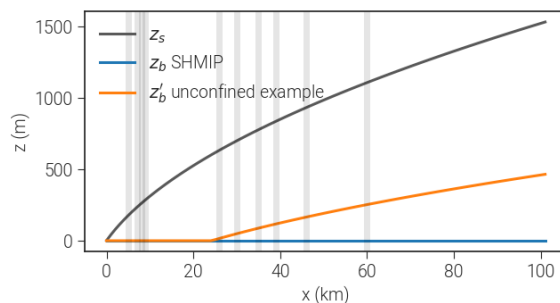

Figure 2. Experiments with artificial geometries. Vertical lines denote moulin positions for SHMIP/B2. The orange line shows the modified bedrock used to illustrate the impact of the confined/unconfined scheme as discussed in Sect. 3.2

In Table 1, we show the physical constants used in all setups and runs. The values in the lower half are properties of the porous medium and are only estimated. Since they are utilized in the context of the equivalent layer model this is not an issue. Table 2 contains the model parameters in the upper part and the variables computed by the model in the lower part.

We divide the sensitivity analysis into a general block investigating the sensitivity to the amount of water input into moulins, the layer thickness b, the confined / unconfined transition parameter d, grid resolution dx (Fig. 3) and a block that examines the parameters directly affecting channel evolution such as channel roughness factor r, creep rate factor A, and bounds for the allowed conductivity $K_{\min}$ and $K_{\max}$ (Fig. 5). In Table 3, we list values that lead to the best agreement with the SHMIP benchmark experiments and thus are used in the following as the baseline for our sensitivity tests.

In Figs. 3a and b, the model's reaction to different amounts of water input through the moulins is shown. With deactivated conductivity evolution ($K = \text{const.}$, dashed lines), larger water inputs lead to higher water pressure, hence lower effective

Table 1. Physical constants used in the model. We distinguish between well known (upper half) and estimated / uncertain (lower half) parameters.

Name	Definition	Value	Units
L	latent heat of fusion	334	$\mathrm{kJ\,kg^{-1}}$
ρ_w	density of water	1000	$\mathrm{kg\,m^{-3}}$
ρ_i	density of ice	910	$\mathrm{kg\,m^{-3}}$
n	flow law exponent	3	-
g	gravitational acceleration	9.81	$\mathrm{m\,s^{-2}}$
β_w	compressibility of water [a]	5.04×10^{-10}	$\mathrm{Pa^{-1}}$
α	compressibility of porous medium[a]	10^{-8}	$\mathrm{Pa^{-1}}$
ω	porosity[a]	0.4	-
S_s	specific storage (Eq. (5))	$\approx 1 \times 10^{-4}$	$\mathrm{m^{-1}}$
S_y	specific yield	0.4	

[a] Values from De Fleurian et al. (2014)

pressure N. In this case, a moulin input of $18\,\mathrm{m^3\,s^{-1}}$ leads to negative values of N. With activated evolution of K, the conductivity adapts to the water input: as more water enters the system through moulins, the conductivity rises. Vertical gray bars show the location of moulins along the x-axis, and the most significant increase in K occurs directly downstream of a moulin. This happens because the water is transported in this direction leading to increased melt. At the glacier snout ($x = 0$),

5 the ice thickness is at its lowest so almost no creep closure takes place; hence, the conductivity reaches its allowed maximum of $0.5\,\mathrm{ms^{-1}}$ for all tested parameter combinations. Significant development of effective drainage is visible for inputs above $2.25\,\mathrm{m^3s^{-1}}$ (yellow line). The resulting effective pressure decreases with rising water input as the system becomes more efficient at removing water. Up to ca. $35\,\mathrm{km}$ distance from the snout this results in almost identical values of N for all forcings above $2.25\,\mathrm{m^3s^{-1}}$. The system adapts so that it can remove all of the additional water efficiently. In Figs. 3i and j, the two-

10 dimensional distributions of N and K are shown for the baseline parameters; in addition, we detail the temporal development of K in Fig. 4.

"Channels" (indicated by regions of high conductivity) form downstream from moulins and continue straight towards the ocean. The effective pressure drops around water inputs and along the "channels".

The layer thickness b directly influences the transmissivity according to Eq. (4). A thicker layer can transport more water

15 out of the system and therefore leads to lower water pressure and higher effective pressure (Figs. 3c and d). At the same time, a thinner layer leads to increased water pressure and higher pressure gradients which results in higher v_melt and can induce negative effective pressure and creep opening.

Table 2. Model parameters (upper) and variables computed in the model (lower)

Name	Definition	Units
$K_{\min}$	min. conductivity	$\mathrm{m\,s^{-1}}$
$K_{\max}$	max. conductivity	$\mathrm{m\,s^{-1}}$
b	aquifer thickness	m
d	confined / unconfined transition (Eq. (6))	m
Q	water supply	$\mathrm{m\,s^{-1}}$
r	roughness factor	-
A	creep rate factor	$\mathrm{Pa^{-3}\,s^{-1}}$
h	hydraulic head	m
K	hydraulic conductivity	$\mathrm{m\,s^{-1}}$
S	storage	-
S_e	effective storage	-
T	transmissivity	$\mathrm{m^2\,s^{-1}}$
v_{melt}	opening by melt	$\mathrm{m\,s^{-2}}$
v_{creep}	opening/closure by creep	$\mathrm{m^{-2}}$
P_{w}	Water pressure	Pa
P_{i}	Ice pressure	Pa
N	effective pressure	Pa

Table 3. Selected baseline parameters for all experiments unless otherwise noted. These parameters best match the SHMIP targets.

Name	Value	Units
$K_{\min}$	0.003	$\mathrm{m\,s^{-1}}$
$K_{\max}$	0.5	$\mathrm{m\,s^{-1}}$
b	10	m
d	0	m
dx	1000	m
r	1	-
A	5×10^{-25}	$\mathrm{Pa^{-3}\,s^{-1}}$
$Q_{\mathrm{per\ moulin}}$	9	$\mathrm{m^3\,s^{-1}}$

The confined–unconfined transition parameter d does not show noticeable effects on the results (Figs. 3e and f) because the experiment has sufficient water input so that all cells are confined in the steady state.
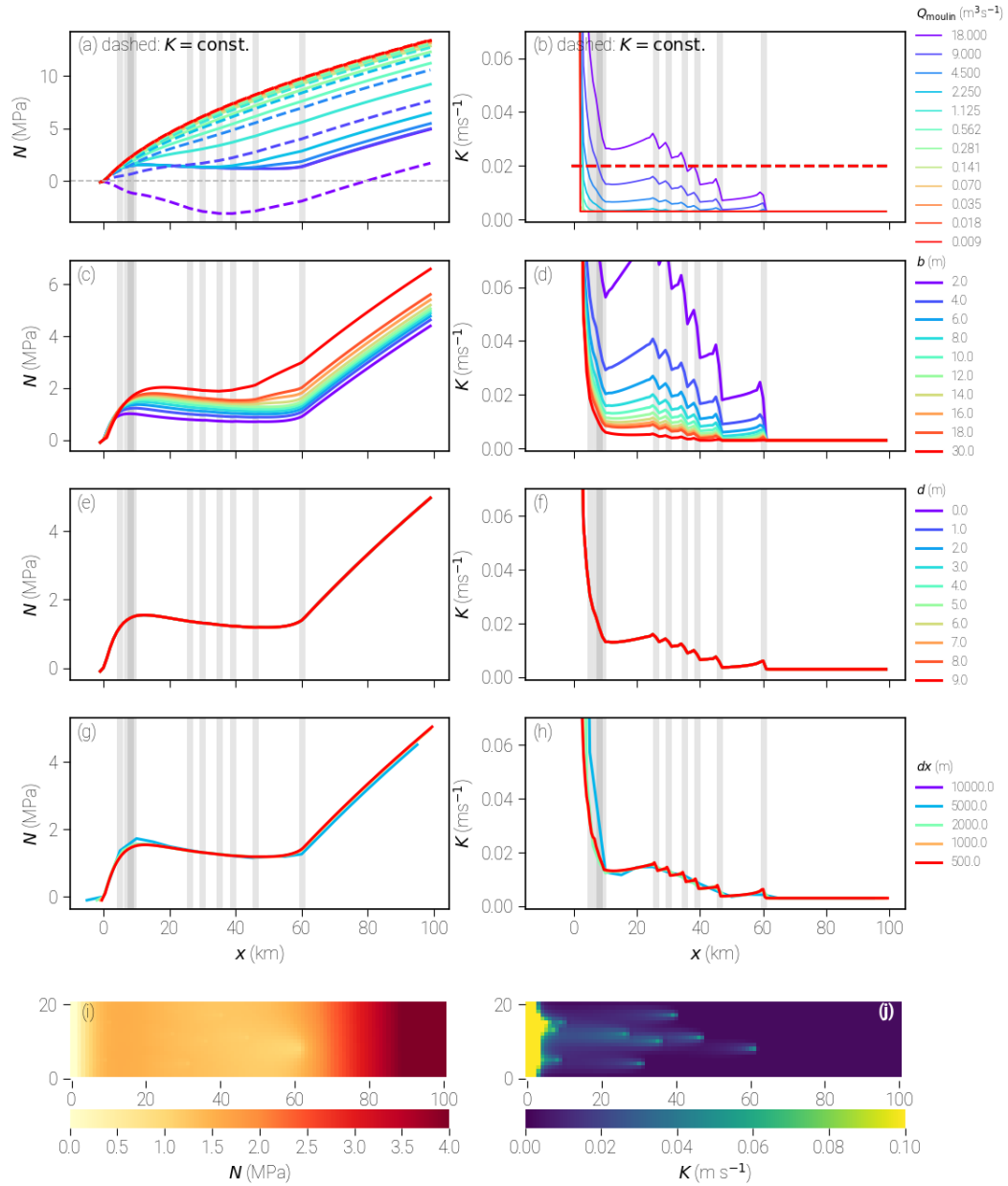
Figure 3. Results from the general sensitivity experiments showing the dependence of N (left) and K (right) on: (a)–(b) Water supply from moulins Q_{moulin} (results for deactivated conductivity evolution are shown using dashed lines), (c)–(d) aquifer layer thickness b, (e)–(f) confined/unconfined transition parameter d, (g)–(h) grid resolution dx. Shown values are averaged along the y-axis to represent cross sections at flow lines. Conductivity plots are cut off at $0.06\,\mathrm{m\,s^{-1}}$ to improve visibility of the relevant range. (i) and (j) show the two-dimensional distributions (map view) of the results using the best-fit baseline parameters.
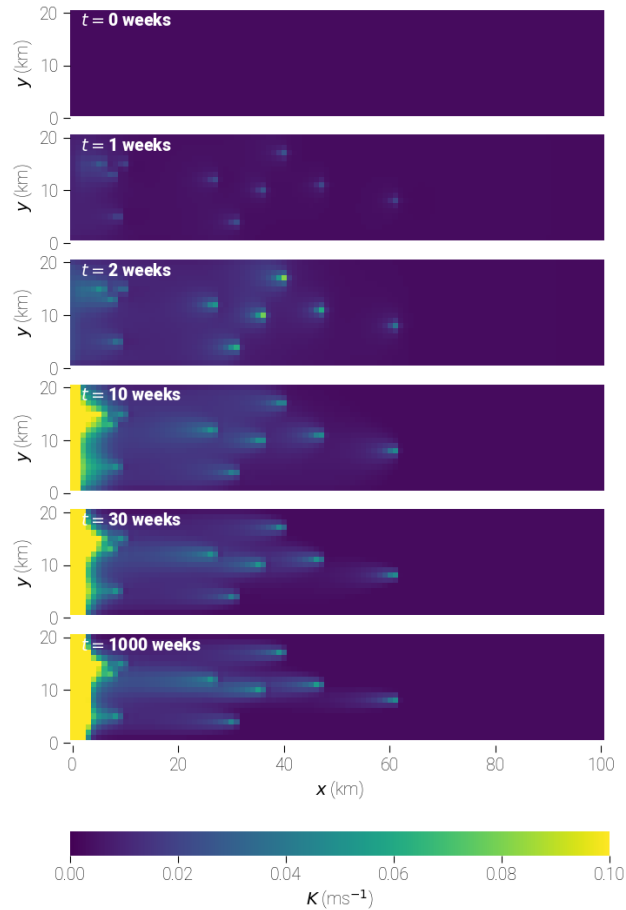
Figure 4. Development of conductivity over time

Grid resolution dx has low influence on the pressure distribution and a minor effect on the conductivity downstream (Figs. 3g and h). However, coarse resolutions are unable to resolve the steps that appear at the moulins.

In Figs. 5a and b, we show the results for different values of $K_{\min}$. $K_{\min}$ ensures that the system is never completely watertight and determines how much water can pass through independently of the system's current state. Higher values lead to more water transport, lower water pressure, and higher effective pressure. In this experiment, values higher than $0.01\,\mathrm{m\,s^{-1}}$ show no reactions of K to moulins upstream of $10\,\mathrm{km}$.

$K_{\max}$ (Fig. 5e and f) has no visible impact on the resulting pressure distribution. The differences in K are only large at the snout, where the maximum is always reached because the ice thickness is too low to counteract the melt term. No significant influence on the upstream area has been detected.

The creep rate factor A determines the "softness" of the ice and therefore effects the creep term in Eq. (9). Larger values of A imply warmer ice; hence, more creep closure (see Figs. 5e and f). Note, that this also effects creep opening if $N < 0$.
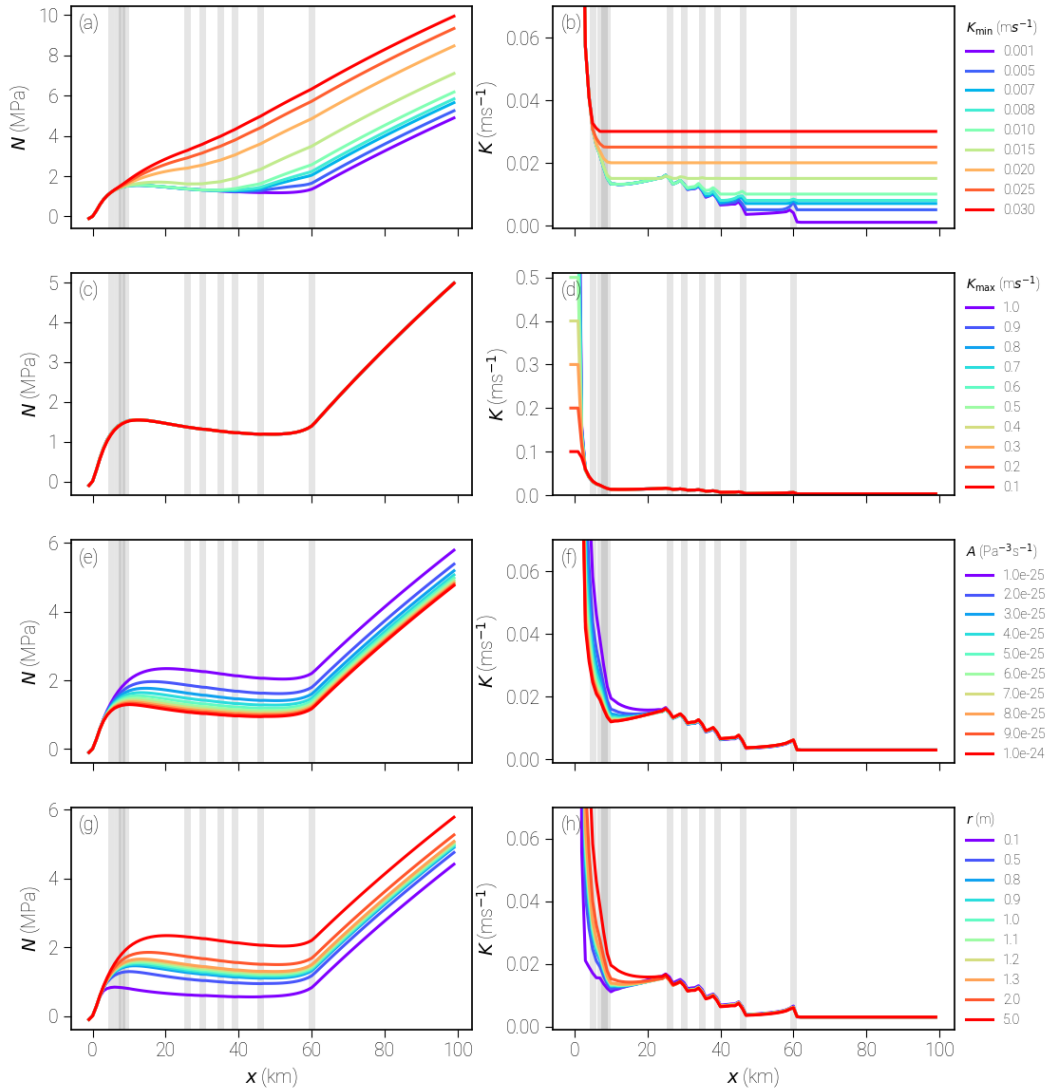
Figure 5. Results from parameters directly related to opening and closure: Limits on the conductivity $K_{\min}$ (panels a and b) and $K_{\max}$ (panels c and d), creep rate factor A (panels e and f) and roughness factor r (panels g and h). Shown values are averaged along the y-axis to represent cross sections at flow lines. Conductivity plots are cut off at $0.06\,\mathrm{ms^{-1}}$ to improve visibility of the relevant range.

The roughness factor r is meant as a measure for small bumps and imperfections, where a rougher "channel" (larger r) would experience more melt because of the larger contact area and more turbulent mixing. Larger values of r lead to higher conductivity and more water transport resulting in lower P_{w} and higher N.

3.2 The benefit from treating unconfined aquifer

As described above, the confined–unconfined aquifer approach is advantageous for obtaining physically meaningful pressure distributions. In the example illustrated in Fig. 6, we use a slightly modified geometry, where the bedrock rises towards the upstream boundary forming a slab $z_b'(x, y) = \max\left(3((x + 5e3)^{1/2} - (5e3)^{1/2}) - 300, 0\right)$. The supply is constant in time and space, and we choose a low value of 7.93e-11 m/s ($\approx$2.5 mm/a) to compare our improved scheme to the simple confined only case. Fig. 6 shows a comparison of the steady state solutions: For the confined-only case, the hydraulic head drops below the bedrock at the upstream region. This results in negative water pressure for these regions. Addressing this by simply limiting the water pressure to zero would result in inconsistencies between the pressure field and the water supply. Our new scheme limits the transmissivity when the head approaches the bedrock and by this means ensures $p_w \geq 0$ in a physically consistent way. Additionally, the confined-only solution completely depends on boundary conditions and supply terms, basal topography has no influence in this case (apart from governing dK/dt). The possibility of the aquifer to become unconfined captures the expected behaviour much better: At high water levels, water pressure distribution dominates water transport, while at low levels the bed topography becomes relevant.
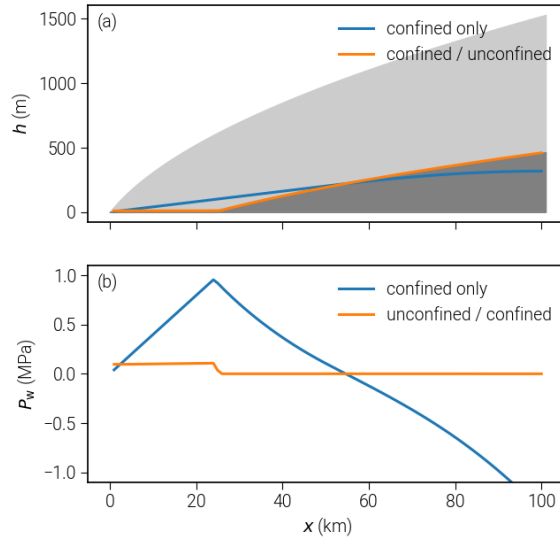

Figure 6. Advantages of using the confined/unconfined aquifer scheme (CUAS): Values of head and water pressure for geometries with non-flat bedrock. (a) Computed head for the confined and combined scheme with ice geometry in the background. In the confined only case, the head goes below bedrock. (b) Resulting water pressure, only for the combined scheme the pressure is always non-negative.

3.3 Seasonal channel evolution and properties

In order to understand our model's ability to simulate the seasonal evolution of subglacial systems, we selected the setup SHMIP/D and ran it with different values of key model parameters. This experiment does not include any moulins but prescribes
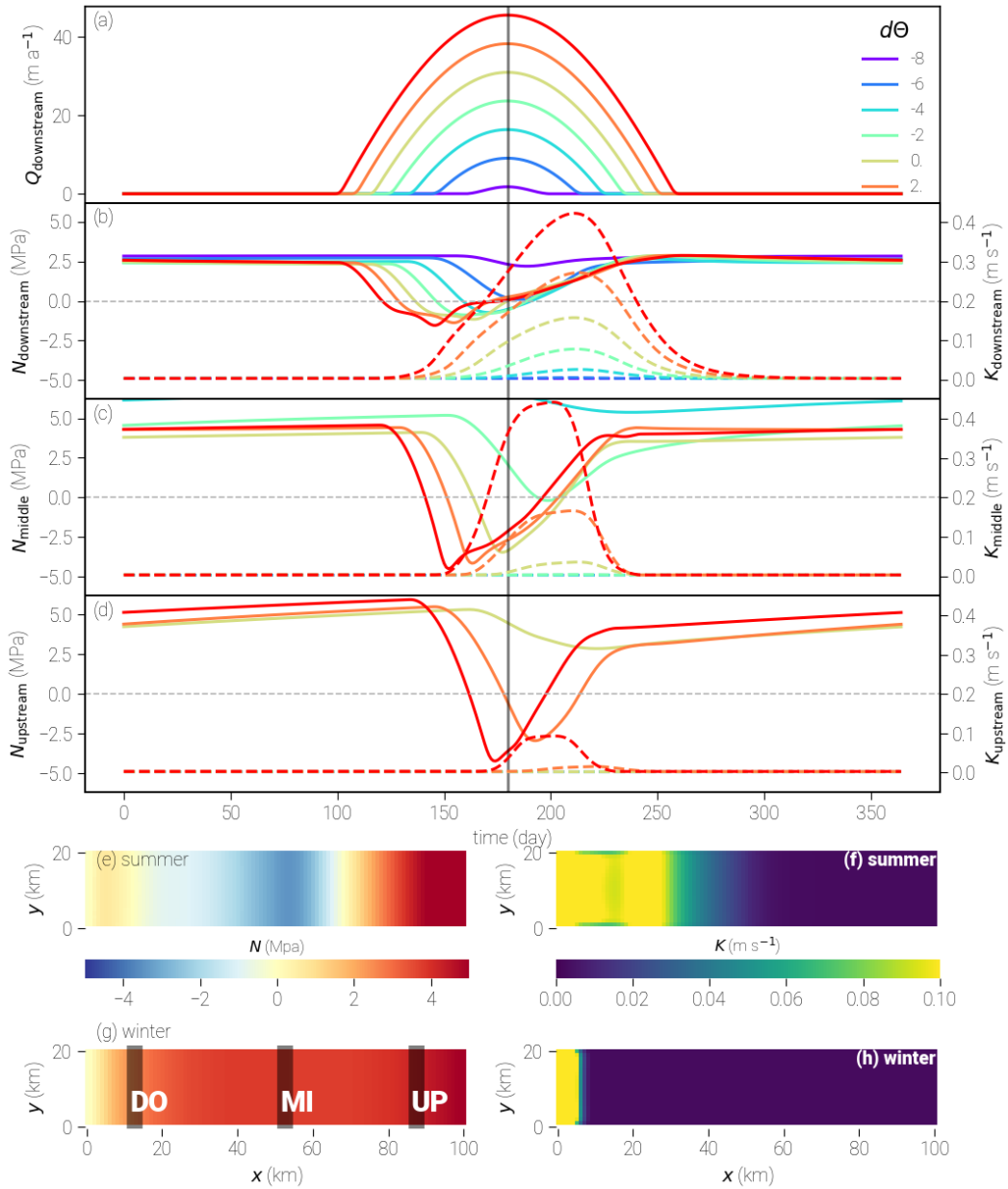
Figure 7. Results for one season of the SHMIP/D experiment. In panels (b)–(d), the left axis (effective pressure) corresponds to the solid lines, while the right axis (conductivity) specifies the values for the dashed lines. The values at the given positions (upstream, middle, downstream) are averaged over the corresponding areas indicated in panel (g). Panels (e)–(h) show two-dimensional distribution maps of $d\Theta = 0$ runs.

a non-uniform spatial distribution of supply instead that also varies seasonally. A simple degree day model with varying temperature parameter $d\Theta$ provides water input rising from the downstream end (lowest elevated) of the glacier towards the

higher elevated areas over summer:

$$\Theta(t) = -16\cos{(2\pi/\text{yr}\,t)} - 5 + d\Theta \tag{12}$$

$$Q_{\text{dist}}(z_s, t) = \max{(0, (z_s\text{LR} + \Theta(t))\text{DDF})} + Q_{\text{basal}}. \tag{13}$$

Here, $\text{yr} = 31536000\,\text{s}$ denotes the number of seconds per year, $\text{LR} = -0.0075\,\text{Km}^{-1}$ the lapse rate, $\text{DDF} = 0.01/86400\,\text{mK}^{-1}\text{s}^{-1}$
is the degree day factor, and $Q_{basal} = 7.93 \times 10^{-11}\,\text{ms}^{-1}$ is additional basal melt. The resulting seasonal evolution of the supply is shown in Fig.7a. The model is run for 10 years so that a periodic evolution of the hydraulic forcing is generated. Here, we present the result for one parameter set only since the model is not very sensitive in this setup. For the prescribed water supplies, the conductivity only reaches its lower limit K_{min} for very short periods, and the upper limit K_{max} is never reached at all (apart from the terminus, where it does not have any significant influence on the upstream behavior of the system as we have shown in the previous experiment).

We chose three different locations to present N and K during the season: downstream of the glacier close to the snout, in the center, and at a far upstream location (Figs. 7b–d; the locations are marked in panel g). Shown time series are spatially averaged over these locations with solid lines representing the effective pressure and dashed lines the conductivity.

Water input increases during the summer months, while the corresponding effective pressure drops. With a time lag the conductivity rises in response. Supply develops from downstream towards the upstream end of the glacier over the season so the decline in N at the downstream location (Fig. 7b) is instantaneous when the supply rises, while at the further inland locations (Figs. 7c and d) N reacts later during the year. At the middle location, the drop in N is more intense almost reaching $-5\,\text{MPa}$ for the temperature parameters of 2 and higher. Temperature parameters below -4 show no response at this location. The same applies to the change in conductivity: only the three highest temperatures lead to a significant rise of K. Finally, at the upstream position, only for $d\Theta = 4$ and $d\Theta = 2$ the effective pressure drops below zero, while for $d\Theta = 0$ the drop is smaller in magnitude and more prolonged. The conductivity rise is only significant for $d\Theta = 4$ at this location. While the onset and minima of the decline in N strongly depend on the amount and timing of the water input for all values of $d\Theta$, the maximum of K and also the time when N returns to winter conditions is similar. For the downstream position, the maximum conductivity is reached for day 210, and N reaches its background value approximately 25 days later. At the center and upstream positions, this behavior is less pronounced but generally similar.

The observed behavior is expected and indicates that our model is able to represent the seasonal evolution of the subglacial water system. Increasing water supply over the year leads to rising water pressure and dropping effective pressure. When the conductivity rises in response, the effective pressure goes up again despite the supply not yet falling again because the more efficient system is able to transport the water away. For the cases, where no visible change in K occurs such as $d\Theta = -6$ (blue line in Fig. 7b), the effective pressure directly follows the supply at the terminus, while at the center position ($d\Theta = -2$, cyan line, Fig. 7c), the minimum is offset by the time needed for the supply to reach that location. The maximum in conductivity K is reached later because once the system becomes efficient, increased water transport stimulates melting that opens the system even more. This self-reinforcing process is only stopped when enough water is removed and the reduced water flux reduces the

melt again. We assume that this leads to similar locations of the conductivity maxima for different $d\Theta$ and the resulting similar reemerging of winter conditions in N.

In this experiment, N becomes negative during the seasonal evolution, which is not physically meaningful. We attribute such behavior to a lack of adjustment of water supply to the state of the system. In reality, the supply from runoff or supraglacial drainage would cease as soon as the pressure in the subglacial water system becomes too high; here we simply continue to pump water into the subglacial system without any feedback. This then leads to negative values of N. It is also consistent with the finding that N becomes negative earlier in the season in cases of higher supply. This deficiency will be addressed in future work.

4 Subglacial hydrology of NEGIS, Greenland

The role of subglacial hydrology in the genesis of ice streams in general is not well understood yet. NEGIS is a very distinct feature of the ice sheet dynamics in Greenland; thus, the question about the role of subglacial water in the genesis of NEGIS is critical. The characteristic increase in horizontal velocities becomes apparent about $100\,\mathrm{km}$ downstream from the ice divide (Vallelonga et al., 2014). Further downstream, the ice stream splits into three different branches: the $79°$ North Glacier (79NG), Zacharias Isbrae (ZI), and Storstrømmen. Thus far, large scale ice models have only been able to capture the distinct flow pattern of NEGIS when using data assimilation techniques such as inverting for the basal friction coefficient (see e.g. horizontal velocity fields in Goelzer et al., 2017). It is assumed that most of the surface velocity can be attributed to basal sliding amplified by basal water instead of ice deformation (Joughin et al., 2001). This means that the addition of a subglacial hydrology might have the potential to improve the results considerably. While many glaciers in Greenland have regularly draining supraglacial lakes and run-off driving a seasonality of the flow velocities, little is known about the effect at NEGIS (Hill et al., 2017). Because of this lack of data, to avoid an increased complexity, and to focus on the question if basal melt alone can account for the development of an efficient system, we do not include any seasonal forcing into our experiment.

Our setup includes the major parts of this system. The pressure adjusted basal temperature Θ_{pmp} obtained from PISM (Aschwanden et al., 2016) is utilized to define the modeling region. We assume that for freezing conditions at the base ($T_{\mathrm{pmp}} < 0.1\,\mathrm{K}$) basal water transport is inhibited and take this as the outline of our model domain. Fig. 8 shows the selected area and PISM basal melt rates used as forcing.

For the ice geometry, we use the bed model of Morlighem et al. (2014) interpolated on a $1.2\,\mathrm{km}$ grid. Boundary conditions at lateral margins are set to no flux, whereas the termini at grounding lines are defined as Dirichlet boundaries with a prescribed head that implies an effective pressure of zero. This means that the water pressure at the terminus is equal to the hydrostatic water pressure of the ocean assuming floating condition for the ice at the grounding line. Parameters used for this experiment are the same as those for the previous experiments (Table 3) but with K_{max} reduced to $0.3\,\mathrm{m\,s^{-1}}$ to speed up the computation. The experiment is run for $50\,\mathrm{a}$ to reach steady state. Despite the large number of cells (444×481), computing time for this setup is still reasonable (48 hours on a single core of Intel Xeon Broadwell E5-2697).
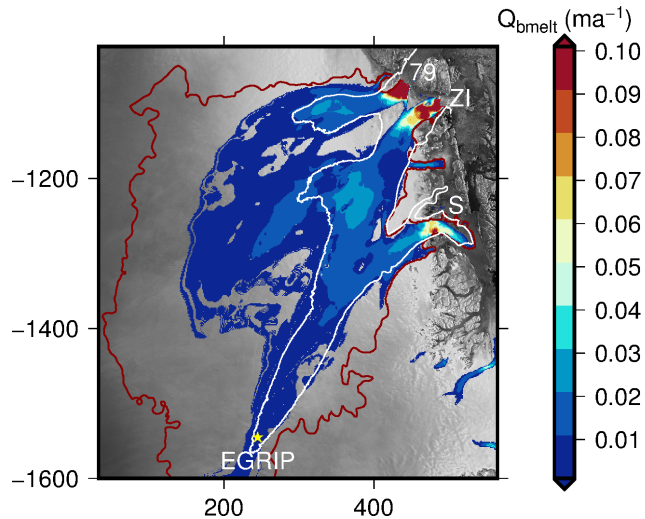
Figure 8. Boundary conditions and forcing for NEGIS experiment. Shown is the basal melt rate from PISM and contour line for $\Theta_{\mathrm{pmp}} = -0.1\,\mathrm{K}$ (red) used as model boundary.

The resulting distributions of effective pressure and conductivity are shown in Figs. 9a and b, respectively. As expected, effective pressure is highest at the ice divide and decreases towards the glacier termini. Conductivity is low for the majority of the study area with the exception of areas in the vicinity of grounding lines and two distinct areas that touch in between 79NG and ZI. The northern area (marked I in Fig. 9b) is located at the northern branch of 79NG and has no direct connection

5 to the snout. The second area (marked II in Fig. 9b) emerges in the transition zone between the southern branch of 79NG and Zacharias Isbrae and covers an area approximately twice as large as area I with higher values of K. It is connected to the snout of ZI with narrow band of high conductivity cells.

Comparing the effective pressure distribution to the observed velocity (Rignot and Mouginot, 2012) – we chose the $50\,\mathrm{ma}^{-1}$ contour line as indicator of fast flow – we observe a high degree of overlap between the fast flowing regions and those with

10 low effective pressure (below $1\,\mathrm{MPa}$) over most of the downstream domain of our study area. Storstrømmen shows slightly higher effective pressure than 79NG and ZI, which is in accordance with lower observed horizontal velocities for that glacier (Joughin et al., 2010). At the onset of the NEGIS, the effective pressure is high, and no relationship to the flow velocity can be observed.

To further examine the possible influence of our hydrology model to basal sliding, we investigate the impact on the sliding

15 law. We chose to compare our computed N_{CUAS} to the reduced ice overburden pressure, defined in Huybrechts (1990) as $N_{\mathrm{HUY}} = P_{\mathrm{i}} + \rho_{\mathrm{sw}}g(z_b - z_{\mathrm{sl}})$ for $z_b < z_{\mathrm{sl}}$ and $N_{\mathrm{HUY}} = P_{\mathrm{i}}$ otherwise.

We show the quotient of H_{HUY} and N_{CUAS} in Fig. 9c. This demonstrates where the application of our hydrology model would increase basal velocities.

In order to demonstrate the effect of the modeled subglacial hydrology system on the NEGIS ice flow, we setup a simple, one-

20 way coupling to an ice flow model. Here, we use the Ice Sheet System Model (ISSM, Larour et al., 2012), an open source finite

16

element flow model appropriate for continental scale and outlet glacier applications (Bondzio et al., 2017; Morlighem et al., 2016). The modeling domain covers the grounded part of the whole NEGIS drainage basin. The ice flow is approximated with the Shallow Ice Approximation (SSA, MacAyeal, 1989; Morland, 1987) within a 2D plan-view model, which is appropriate for fast flowing ice but not for the slow flowing parts in our model area. Since we aim do demonstrate that our addition of the hydrology model improves results in fast flowing areas where the SSA is valid, this is not a huge concern. As we use the SSA we do not perform a thermo-mechanical coupling but prescribe a depth-averaged hardness factor in Glens flow law. Model calculations are performed on an unstructured finite element grid with a high resolution of $1\,\mathrm{km}$ in fast flow regions and coarse resolution of $20\,\mathrm{km}$ in the interior. The basal drag $\boldsymbol{\tau}_b$ is written in a Coulomb-like friction law:

$$\boldsymbol{\tau}_b = -k^2 N \mathbf{v}_b, \tag{14}$$

where $\mathbf{v}_b$ is the basal velocity vector tangential to the glacier base, N the effective pressure, and k^2 a positive constant. We run two different scenarios, where (1) the effective pressure is parametrized as the reduced ice overburden pressure, $N = N_{\mathrm{HUY}}$, and (2) the effective pressure distribution is taken from the hydrological model at steady state, $N = N_{\mathrm{CUAS}}$. The value of k^2 is tuned in order to have ice velocities of approximately $1500\,\mathrm{ma}^{-1}$ at the grounding line at the 79NG. For both scenarios, the value of k^2 is $0.1\,\mathrm{sm}^{-1}$. The results for both scenarios are shown in Fig. 10a and c, respectively. Additionally, we show the observed velocities (Fig. 10d, Rignot and Mouginot, 2012) and the PISM surface velocities (Fig. 10b, Aschwanden et al., 2016). Note that the latter is a PISM model output on a regular grid interpolated to the unstructured ISSM grid.

Velocities computed with the reduced ice overburden pressure are generally too slow and do not resemble the structure of the fast flowing branches at all. The result from PISM shows distinct branches for the different glaciers, which display a relatively sharp separation from the surrounding area. Note, that PISM also uses a basal hydrology model as described in Bueler and van Pelt (2015). Velocities are slightly lower than observed velocities, especially for Zacharias Isbrae and in the area, where ZI and 79NG are closest. In the upper part towards the ice divide, the ice stream structure is not visible in the velocities. The ISSM model using effective pressure computed by CUAS produces high velocities towards the ocean that closely resemble N. The transition between the ice streams and the surrounding ice is poorly reproduced. While the stream structure is way too diffused, the velocity magnitude for the glaciers appears reasonable. The inland part is similar to observed velocities but – as in the PISM simulation – the upper part where NEGIS is initiated is not present. The onset of NEGIS is thought to be controlled by high local anomalies in the geothermal flux (Fahnestock et al., 2001), which PISM currently does not account for. Higher geothermal flux would lead to more basal melt, hence, water supply in the hydrology model. However, the consequences for the modeled effective pressure would require further experiments which are not in the scope of this paper.

In Tab. 4 we show the root mean square error ($l2$-norm), Pearson correlation coefficient r^1 and Δv ($l1$-norm) between the modeled and observed velocities.

We find it impressive that even without extensive tuning, we can considerably improve the velocity field in ISSM by our simple one-way coupling to the hydrology model. However, the results in this section are to be understood not as a thorough study of the NEGIS but as a first application of the model to a real geometry. A complete study requires extended observations in order to determine the optimal model parameters. However, we are confident that our results represent the general aspects of

Table 4. Comparison of modeling results for ice velocity to observed values (Rignot and Mouginot, 2012). Herein RMS denotes the root mean square error or $l2$-norm, r^2 is the Pearson correlation coefficient and ΔV is the $l1$-norm.

	RMS (ma^{-1})	r^2	Δv (ma^{-1})
ISSM with reduced ice overburden pressure	176.83	0.69	90.13
PISM (Aschwanden et al., 2016)	132.05	0.84	65.42
ISSM with N computed from CUAS	126.86	0.80	53.28

the hydrological system at NEGIS. Based on our sensitivity and seasonal experiments (Sect. 3.1 and Sect. 3.3) we expect the high-conductivity-areas to be a stable feature, which would extend or retract depending on the chosen values of the melt and creep parametrizations but not change their location. Available supply plays a more important role here, and we assume that different basal melt distributions – or the addition of surface melt – might considerably change the position and the extent of the efficient system and, therefore, the effective pressure distribution as can be seen in Sect. 3.3.

The onset of NEGIS is not well reproduced in the PISM simulation as well as in our ISSM result. Since the ice is slow in the PISM results in that area, basal melt rates are low, and, since we use these as input in our hydrology model, it is expected that our model computes low water pressure here. In our opinion this another point of having a real two-way coupling between the ice model and the basal hydrology model in order to obtain good results. These results could then in turn be used to guide further optimization of the modeling parameters in our hydrology model in the future.

5 Conclusions

We present the first equivalent aquifer layer model for subglacial hydrology that includes the treatment of unconfined water flow. It uses only a single water layer with adaptive conductivity. Since extensive observations of the subglacial system are rare, its relative simplicity and empirical nature can be an advantage.

We find strong model sensitivity to the lower limit of conductivity $K_{\min}$, grid spacing dx, and the parametrization of melt v_{melt} and creep v_{creep}, while the sensitivity to the upper limit of conductivity $K_{\max}$ and the confined–unconfined transition parameter d is low. Our model robustly reproduces the seasonal cycle with the development and decline of the effective system over the year. Another positive aspect of our modeling approach was the complete absence of instabilities similar to those arising due to runaway channel enlagement – even at high flow rates. We attribute this fact that our combined confined/unconfined aquifer model quickly transports excess water away from confined aquifer parts, where high water pressure could lead to steep increases in effective conductivity (via negativ v_{creep} term).

In our NEGIS experiments, we find the presence of a partial efficient system for winter conditions. The distribution of effective pressure broadly agrees with observed velocities, while the upstream part is not represented correctly. When coupled to ISSM, our hydrology model notably improves computed velocities.

A number of aspects of the proposed model can be further developed; those include improved parametrizations of several physical mechanisms (e.g. adding feedback between pressure and water supplies), changing the hydraulic conductivity coefficient to a tensor-valued on to better represent the anisotropy of channel networks, and, last but not least, transition to a mixed formulation of the Darcy equation discretized on an unstructured mesh in order to preserve mass conservation and to improve resolution in the areas of interest.

Appendix A: Parametrization of evolution of conductivity

We use the same parametrization as de Fleurian et al. (2016) detailed here using the notation in Cuffey and Paterson (2010).

Creep term

Nye (1976), found for the closure on channels due to creep that

$$\frac{1}{R_c}\frac{\partial R_c}{\partial t} = A\left[\frac{N}{n}\right]^n, \tag{A1}$$

with R_c denoting the channel radius and A_c the channel area ($= \pi R_c^2$) (notation as in (Cuffey and Paterson, 2010, Eq. 6.15)). Multiplication by $2\pi\rho_i R_c^2 = 2\rho_i A_c$ on both sides, leads to

$$2\pi\rho_i R_c \frac{\partial R_c}{\partial t} = 2\rho_i A_c A\left[\frac{N}{n}\right]^n \tag{A2}$$

Rewriting the left side to area, using the chain rule ($\frac{\partial A_c}{\partial t} = 2\pi \frac{\partial R_c}{\partial t}$) yields

$$\rho_i \frac{\partial A_c}{\partial t} = 2\rho_i A_c A\left[\frac{N}{n}\right]^n. \tag{A3}$$

Melt term

Heat produced over ds in unit time is $Q_w G$ and pressure melting point effects are $\rho_w Q_w c_w \mathcal{B}\frac{dP_i}{ds}$, which leads to

$$\dot{M}L_f = \underbrace{Q_w G}_{\text{turb. heat produced}} - \underbrace{\rho_w Q_w c_w B \frac{dP_i}{ds}}_{\text{PMP effect}} \tag{A4}$$

(Cuffey and Paterson, 2010, Eq. 6.16), where $\dot{M}$ represents the melt rate (mass per unit length of wall in unit time) and the magnitude of gradient of the hydraulic potential is given by

$$G = |\nabla\phi_h|, \quad \text{where} \quad \phi_h = \rho_w g h. \tag{A5}$$

Neglecting the PMP effects we get

$$\dot{M} = \frac{Q_w G}{L_f} \tag{A6}$$

using $Q_w = qb$ (confined case, unconfined would be $Q_w = q(h - z_b)$) and $q = K\nabla(h)$ (ommiting the minus, because we need the magnitude here) this is

$$\dot{M} = \frac{K\nabla(h)b\nabla(\rho_w g h)}{L_f} \tag{A7}$$

which can be rewritten to

$$\dot{M} = \frac{\rho_w g K b (\nabla h)^2}{L_f}. \tag{A8}$$

Opening and closure

The conduit expands when there is more melt than ice inflow due to creep

$$\rho_i \frac{\partial A_c}{\partial t} = \dot{M} - \underbrace{2\rho_i A_c A \left[\frac{N}{n}\right]^n}_{\text{creep term from A3}} \tag{A9}$$

(Cuffey and Paterson, 2010, Eq. 6.42). Inserting $\dot{M}$ from Eq. A8 and dividing by ρ_i results in

$$\frac{\partial A_c}{\partial t} = \frac{\rho_w g K b (\nabla h)^2}{L_f \rho_i} - 2 A_c A \left[\frac{N}{n}\right]^n. \tag{A10}$$

Change of area to conductivity

This is a purely geometrical argument, since we are interested in the transmissivity $T = Kb$ ($T = Kh$ for unconfined) and therefore, a change in K is equivalent to a change in the aquifer thickness b.

Hence, we add a roughness term r to be able to investigate the sensitivity of our model to the melt term and write

$$\frac{\partial K}{\partial t} = \frac{r g \rho_w b K (\nabla h)^2}{L_f \rho_i} - 2 K A \left[\frac{N}{n}\right]^n \tag{A11}$$

and considering unconfined case as well, it is

$$\frac{\partial K}{\partial t} = \frac{r g \rho_w \min(b, h - z_b) K (\nabla h)^2}{L_f \rho_i} - 2 K A \left[\frac{N}{n}\right]^n. \tag{A12}$$

Our reasoning behind scaling K and not b are unintended side effects of changes in b on storage and the behaviour when the aquifer becomes unconfined. A thicker aquifer in areas which represent channels would imply larger storage and also less transmissivity when the area eventually becomes unconfined (because the unconfined case triggers at a higher head already, limiting transmissivity). However, we do not expect the storage to increase, because channels usually do not store a lot of water and pressure changes travel faster than in the inefficient system. Also, the effective system should still have higher transmissivity when the water pressure drops (as long as it does not empty completely).

Appendix B: Discretization

We discretize the transient flow equation (Eq. (3)) on an equidistant rectangular grid using an explicit forward in time central in space (FTCS) finite-difference approximation. For sake of completeness, we give the equations for a non-equidistant grid here.

For the spatial discretization, we use a second-order central difference scheme (e.g., Ferziger and Perić, 2002) leading to the spatial discretization operator for the head $\mathcal{L}_h$:

$$\mathcal{L}_h = T_{i+\frac{1}{2},j} \frac{h_{i+1,j} - h_{i,j}}{(\Delta_f x)_i (\Delta_c x)_i} - T_{i-\frac{1}{2},j} \frac{h_{i,j} - h_{i-1,j}}{(\Delta_b x)_i (\Delta_c x)_i}$$
$$+ T_{i,j+\frac{1}{2}} \frac{h_{i,j+1} - h_{i,j}}{(\Delta_f y)_j (\Delta_c y)_j} - T_{i,j-\frac{1}{2}} \frac{h_{i,j} - h_{i,j-1}}{(\Delta_b 1)_j (\Delta_c y)_j} + Q \tag{B1}$$

5   where half-grid values of T denote harmonic rather than arithmetic averages computed using Eq. (4), where

$$(\Delta_c x)_k = (x_{k+1} - x_{k-1})/2, \tag{B2}$$

$$(\Delta_f x)_k = x_{k+1} - x_k, \quad \text{and} \tag{B3}$$

$$(\Delta_b x)_k = x_k - x_{k-1} \tag{B4}$$

denote central, forward, and backward differences, respectively. Re-writing this more compactly in compass notation

10   $$\mathcal{L}_h = d_S h_S + d_W h_W + d_P h_P + d_E h_E + d_N h_N + Q \tag{B5}$$

with

$$d_W = \frac{T_{i-\frac{1}{2},j}}{(\Delta x)_i^2}, \quad d_E = \frac{T_{i+\frac{1}{2},j}}{(\Delta x)_i^2}, \quad d_S = \frac{T_{i,j-\frac{1}{2}}}{(\Delta x)_j^2}, \quad d_N = \frac{T_{i,j+\frac{1}{2}}}{(\Delta x)_j^2},$$

and $\quad d_P = -(d_W + d_E + d_S + d_N).$ \tag{B6}

We use the explicit Euler method for the time discretization, where the next time step $m+1$ is computed from the previous
15   time step m ($\Delta t = t_{m+1} - t_m$) (using a somewhat sloppy notation)

$$h^{m+1} = h^m + \frac{\Delta t}{S_e} (d_S^m h_S^m + d_W^m h_W^m$$
$$+ d_P^m h_P^m + d_E^m h_E^m + d_N^m h_N^m - Q^m). \tag{B7}$$

Conductivity is updated in each time step by Eq. (9):

$$K^{m+1} = K^m + \Delta t \left(v_{\text{melt}}^m - v_{\text{creep}}^m \right), \tag{B8}$$

20   where we use a combined forward- backward-difference scheme for the discretization of $(\nabla h)^2$ in Eq. (10):

$$(\nabla h)^2 \approx \frac{1}{2} \left[\left(\frac{h_{i,j} - h_{i-1,j}}{(\Delta_b x)_i} \right)^2 + \left(\frac{h_{i+1,j} - h_{i,j}}{(\Delta_f x)_i} \right)^2 \right.$$
$$\left. + \left(\frac{h_{i,j} - h_{i,j-1}}{(\Delta_b y)_j} \right)^2 + \left(\frac{h_{i,j+1} - h_{i,j}}{(\Delta_f y)_j} \right)^2 \right]. \tag{B9}$$

Compared to central differences, this stencil is more robust at nodes with large heads caused by moulins.

The time step is chosen sufficiently small that the discretization error is dominated by the spatial discretization (the Courant–Friedrichs–L condition is always satisfied) Additionally, we check that the time step is small enough for the unconfined component of the scheme to become active by restarting the time step with a decreased Δt if at any point $h < z_b$.

5 All variables are co-located on the same grid, but the conductivity K is evaluated at the midpoints between two grid cells using the harmonic mean due to its better representation of conductivity jumps (e.g. at no-flow boundaries).

A disadvantage of this discrete formulation is that it is not mass-conservative (see, e.g. Celia et al. (1990)). The solution to this is to use a mixed formulation for Darcy flow in which also the Darcy velocity is solved for. However, in our application, the resulting error is very small, and we plan to implement the mixed formulation approach in future work.

References

Aschwanden, A., Fahnestock, M. A., and Truffer, M.: Complex Greenland outlet glacier flow captured, Nature Communications, 7, https://doi.org/10.1038/ncomms10524, 2016.

Bartholomew, I., Nienow, P., Mair, D., Hubbard, A., King, M. A., and Sole, A.: Seasonal evolution of subglacial drainage and acceleration in a Greenland outlet glacier, Nature Geoscience, 3, 408–411, 2010.

Bondzio, J. H., Morlighem, M., Seroussi, H., Kleiner, T., Rückamp, M., Mouginot, J., Moon, T., Larour, E. Y., and Humbert, A.: The mechanisms behind Jakobshavn Isbræ's acceleration and mass loss: A 3-D thermomechanical model study, Geophysical Research Letters, 44, 6252–6260, https://doi.org/10.1002/2017GL073309, 2017GL073309, 2017.

Bueler, E. and van Pelt, W.: Mass-conserving subglacial hydrology in the Parallel Ice Sheet Model version 0.6, Geoscientific Model Development, 8, 1613–1635, https://doi.org/10.5194/gmd-8-1613-2015, http://www.geosci-model-dev.net/8/1613/2015/, 2015.

Celia, M. A., Bouloutas, E. T., and Zarba, R. L.: A general mass-conservative numerical solution for the unsaturated flow equation, Water Resources Research, 26, 1483–1496, https://doi.org/10.1029/WR026i007p01483, http://dx.doi.org/10.1029/WR026i007p01483, 1990.

Cuffey, K. M. and Paterson, W. S. B.: The physics of Glaciers, Elsevier, Oxford, 4th edn., 2010.

De Fleurian, B., Gagliardini, O., Zwinger, T., Durand, G., Le Meur, E., Mair, D., and Raback, P.: A double continuum hydrological model for glacier applications, Cryosphere, 8, 137–153, https://doi.org/10.5194/tc-8-137-2014, 2014.

de Fleurian, B., Morlighem, M., Seroussi, H., Rignot, E., van den Broeke, M. R., Kuipers Munneke, P., Mouginot, J., Smeets, P. C. J. P., and Tedstone, A. J.: A modeling study of the effect of runoff variability on the effective pressure beneath Russell Glacier, West Greenland, Journal of Geophysical Research: Earth Surface, 121, 1834–1848, https://doi.org/10.1002/2016JF003842, http://dx.doi.org/10.1002/2016JF003842, 2016JF003842, 2016.

Ehlig, C. and Halepaska, J. C.: A numerical study of confined-unconfined aquifers including effects of delayed yield and leakage, Water Resources Research, 12, 1175–1183, https://doi.org/10.1029/WR012i006p01175, http://dx.doi.org/10.1029/WR012i006p01175, 1976.

Fahnestock, M., Abdalati, W., Joughin, I., Brozena, J., and Gogineni, P.: High geothermal heat flow, basal melt, and the origin of rapid ice flow in central Greenland, Science, 294, 2338–2342, https://doi.org/10.1126/science.1065370, 2001.

Ferziger, J. H. and Perić, M.: Computational Methods for Fluid Dynamics, Springer, 3rd edn., 2002.

Flowers, G. E.: Modelling water flow under glaciers and ice sheets, Proceedings of the Royal Society A-mathematical Physical and Engineering Sciences, 471, 20140907, https://doi.org/10.1098/rspa.2014.0907, 2015.

Fowler, A. C.: Sliding with cavity formation, Journal of Glaciology, 33, 255–267, https://doi.org/10.1017/S0022143000008820, 1987.

Gimbert, F., Tsai, V. C., Amundson, J. M., Bartholomaus, T. C., and Walter, J. I.: Subseasonal changes observed in subglacial channel pressure, size, and sediment transport, Geophysical Research Letters, 43, 3786–3794, 2016.

Goelzer, H., Nowicki, S., Edwards, T., Beckley, M., Abe-Ouchi, A., Aschwanden, A., Calov, R., Gagliardini, O., Gillet-Chaulet, F., Golledge, N. R., Gregory, J., Greve, R., Humbert, A., Huybrechts, P., Kennedy, J. H., Larour, E., Lipscomb, W. H., Le clec'h, S., Lee, V., Morlighem, M., Pattyn, F., Payne, A. J., Rodehacke, C., Rückamp, M., Saito, F., Schlegel, N., Seroussi, H., Shepherd, A., Sun, S., van de Wal, R., and Ziemen, F. A.: Design and results of the ice sheet model initialisation experiments initMIP-Greenland: an ISMIP6 intercomparison, The Cryosphere Discussions, 2017, 1–42, https://doi.org/10.5194/tc-2017-129, https://www.the-cryosphere-discuss.net/tc-2017-129/, 2017.

Hewitt, I. J.: Seasonal changes in ice sheet motion due to melt water lubrication, Earth and Planetary Science Letters, 371, 16–25, https://doi.org/10.1016/j.epsl.2013.04.022, 2013.

Hewitt, I. J., Schoof, C., and Werder, M. A.: Flotation and free surface flow in a model for subglacial drainage. Part 2. Channel flow, Journal of Fluid Mechanics, 702, 157–187, https://doi.org/10.1017/jfm.2012.166, 2012.

Hill, E. A., Carr, J. R., and Stokes, C. R.: A Review of Recent Changes in Major Marine-Terminating Outlet Glaciers in Northern Greenland, Frontiers in Earth Science, 4, 111, https://doi.org/10.3389/feart.2016.00111, https://www.frontiersin.org/article/10.3389/feart.2016.00111, 2017.

Hoffman, M. and Price, S.: Feedbacks between coupled subglacial hydrology and glacier dynamics, Journal of Geophysical Research-earth Surface, 119, 414–436, https://doi.org/10.1002/2013JF002943, 2014.

Hubbard, B., Sharp, M., Willis, I., NIELSEN, M. t., and Smart, C.: Borehole water-level variations and the structure of the subglacial hydrological system of Haut Glacier d'Arolla, Valais, Switzerland, Journal of Glaciology, 41, 572–583, 1995.

Huybrechts, P.: A 3-D model for the Antarctic ice sheet: a sensitivity study on the glacial-interglacial contrast, Climate Dynamics, 5, 79–92, 1990.

Joughin, I., Fahnestock, M., MacAyeal, D., Bamber, J. L., and Gogineni, P.: Observation and analysis of ice flow in the largest Greenland ice stream, Journal of Geophysical Research: Atmospheres, 106, 34 021–34 034, 2001.

Joughin, I., Smith, B. E., Howat, I. M., Scambos, T., and Moon, T.: Greenland flow variability from ice-sheet-wide velocity mapping, Journal of Glaciology, 56, 415–430, 2010.

Kolditz, O., Shao, H., Wang, W., and Bauer, S., eds.: Thermo-Hydro-Mechanical-Chemical Processes in Fractured Porous Media: Modelling and Benchmarking, Springer, 2015.

Larour, E., Seroussi, H., Morlighem, M., and Rignot, E.: Continental scale, high order, high spatial resolution, ice sheet modeling using the Ice Sheet System Model (ISSM), Journal of Geophysical Research: Earth Surface, 117, https://doi.org/10.1029/2011JF002140, 2012.

Lliboutry, L.: General theory of subglacial cavitation and sliding of temperate glaciers, Journal of Glaciology, 7, 21–58, 1968.

MacAyeal, D. R.: Large-scale ice flow over a viscous basal sediment: Theory and application to ice stream B, Antarctica, Journal of Geophysical Research: Solid Earth, 94, 4071–4087, 1989.

Morland, L.: Unconfined ice-shelf flow, Dynamics of the West Antarctic Ice Sheet, 4, 99–116, 1987.

Morlighem, M., Rignot, E., Mouginot, J., Seroussi, H., and Larour, E.: Deeply incised submarine glacial valleys beneath the Greenland ice sheet, Nature Geoscience, 7, 418–422, 2014.

Morlighem, M., Bondzio, J., Seroussi, H., Rignot, E., Larour, E., Humbert, A., and Rebuffi, S.: Modeling of Store Gletscher's calving dynamics, West Greenland, in response to ocean thermal forcing, Geophysical Research Letters, 43, 2659–2666, https://doi.org/10.1002/2016gl067695, 2016.

Nye, J. F.: Water flow in glaciers: Jökulhlaups, tunnels and veins, Journal of Glaciology, 17, 181–207, 1976.

Rignot, E. and Mouginot, J.: Ice flow in Greenland for the international polar year 2008–2009, Geophysical Research Letters, 39, 2012.

Rothlisberger, H.: Water pressure in subglacial channels, in: Union Géodésique et Géophysique Internationale. Association Internationale d'Hydrologie Scientifique. Commission de Neiges et Glaces. Symposium on the hydrology of Glaciers, Cambridge, 7, p. 97, 1969.

Röthlisberger, H.: Water Pressure in Intra- and Subglacial Channels, Journal of Glaciology, 11, 177–203, https://doi.org/10.1017/S0022143000022188, 1972.

Schoof, C.: Ice-sheet acceleration driven by melt supply variability, Nature, 468, 803–806, http://dx.doi.org/10.1038/nature09618, 2010.

Schoof, C., Hewitt, I. J., and Werder, M. A.: Flotation and free surface flow in a model for subglacial drainage. Part 1. Distributed drainage, Journal of Fluid Mechanics, 702, 126–156, 2012.

Shreve, R.: Movement of water in glaciers, Journal of Glaciology, 11, 205–214, 1972.

Vallelonga, P., Christianson, K., Alley, R. B., Anandakrishnan, S., Christian, J. E. M., Dahl-Jensen, D., Gkinis, V., Holme, C., Jacobel, R. W., Karlsson, N. B., Keisling, B. A., Kipfstuhl, S., Kjær, H. A., Kristensen, M. E. L., Muto, A., Peters, L. E., Popp, T., Riverman, K. L., Svensson, A. M., Tibuleac, C., Vinther, B. M., Weng, Y., and Winstrup, M.: Initial results from geophysical surveys and shallow coring of the Northeast Greenland Ice Stream (NEGIS), The Cryosphere, 8, 1275–1287, https://doi.org/10.5194/tc-8-1275-2014, https://www.the-cryosphere.net/8/1275/2014/, 2014.

van den Broeke, M., Box, J., Fettweis, X., Hanna, E., Noël, B., Tedesco, M., van As, D., van de Berg, W. J., and van Kampenhout, L.: Greenland Ice Sheet Surface Mass Loss: Recent Developments in Observation and Modeling, Current Climate Change Reports, pp. 1–12, 2017.

Van Siclen, C. D.: Equivalent channel network model for permeability and electrical conductivity of fracture networks, Journal of Geophysical Research: Solid Earth, 107, ECV 1–1–ECV 1–10, https://doi.org/10.1029/2000JB000057, http://dx.doi.org/10.1029/2000JB000057, 2002.

Weertman, J.: On the sliding of glaciers, J. Glaciol, 3, 33–38, 1957.

Werder, M. A., Hewitt, I. J., Schoof, C. G., and Flowers, G. E.: Modeling channelized and distributed subglacial drainage in two dimensions, Journal of Geophysical Research-earth Surface, 118, 2140–2158, https://doi.org/10.1002/jgrf.20146, 2013.
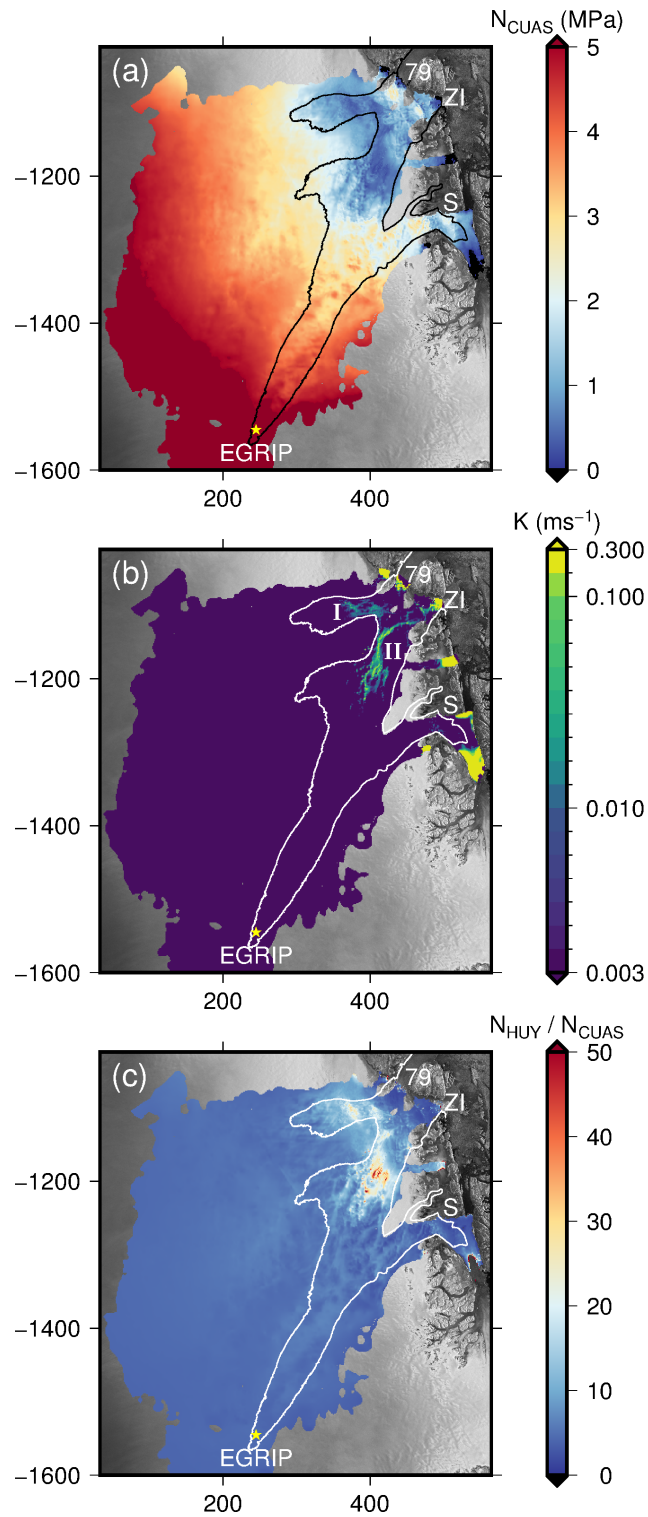
Figure 9. Results for NEGIS region with forcing due to basal melt (PISM) representing winter conditions. White lines indicate the $50\,\mathrm{ma}^{-1}$ velocity contour. Panel (a) shows effective pressure N_{CUAS}, (b) conductivity K (logarithmic scale), and (c) shows the quotient of the ice overburden pressure above flotation and the effective pressure computed by CUAS.
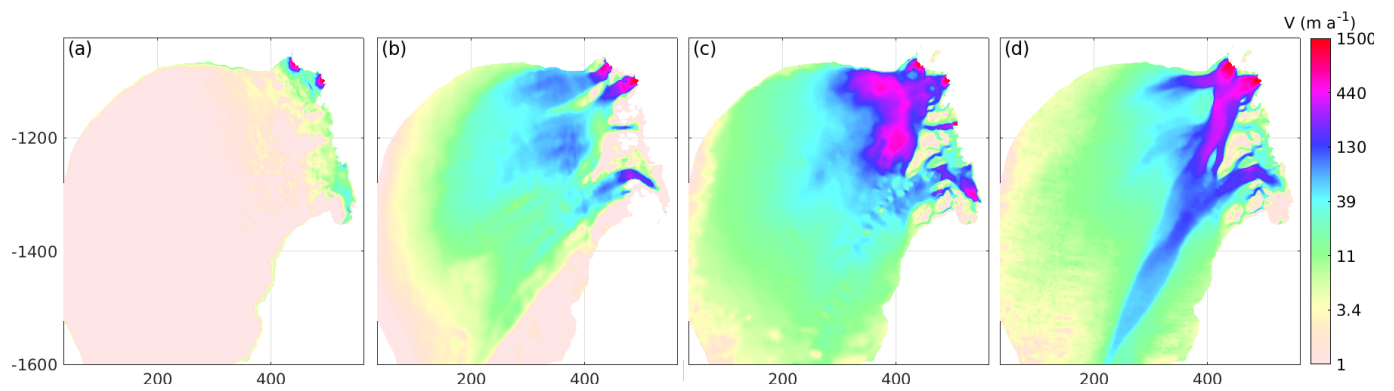
26

Figure 10. Horizontal surface velocity: ISSM with reduced ice overburden pressure N_{HUY} (a), PISM result from Aschwanden et al. (2016), interpolated to unstructured ISSM grid (b), ISSM with effective pressure from our hydrology model N_{CUAS} (c), and observed velocities (Rignot and Mouginot, 2012) (d).